GMR
The Original

SIO_2/G-C_3N_4 NANOCOMPOSITE-ENABLED IMMUNOSENSOR PLATFORM FOR HIGH-FIDELITY ELECTROCHEMICAL DETECTION OF ALPHA-FETOPROTEIN

Samiksha Antil[1], Saravjeet Singh[2*]

[1,2] Department of Biomedical Engineering, Deenbandhu Chhotu Ram University of Science and Technology, Murthal 131039, India
*Corresponding author, E-mail address: *saravjeet.bme@dcrustm.org

ABSTRACT

A selective and highly sensitive electrochemical AFP immunosensor was developed using SiO_2/g-C_3N_4 nanocomposite as the sensing element. α-fetoprotein (AFP) is widely known as a biomarker for the early clinical diagnosis of liver cancer. The SiO_2/g-C_3N_4 was synthesized by the hydrothermal method, and the crystallinity, chemical bond, optical property, morphology, and composition of the prepared composite were studied using X-ray diffraction (XRD), Fourier transform infra-red (FTIR), UV-Vis, scanning electron microscope (SEM) and energy-dispersive spectroscopy (EDS). The high density of active sites on the nanocomposite allows stabilize binding of the anti-AFP antibody, and the binding of AFP with the anti-AFP antibody, results in immune complex layer formation on the electrode's surface. The electrochemical performance of SiO_2/g-C_3N_4 nanocomposite was examined thoroughly, along with the electrochemical response signals following the immune reaction between AFP and its antibody. The proposed immunosensor exhibited a linear response to lgc_{AFP} within the concentration range of 0.25-500 ng/mL with a detection limit of 0.0024 ng/mL.The developed immunosensor showed high reproducibility and retained more than 92.6% of the initial response after storage for 28 days at 4°C. The immunosensor developed has great potential for clinical application and further development in the area of hepatocellular carcinoma (HCC) monitoring.

KEYWORDS: Alpha-fetoprotein, Electrochemical immunosensor, Hepatocellular carcinoma, Nanocomposite, SiO_2/g-C_3N_4

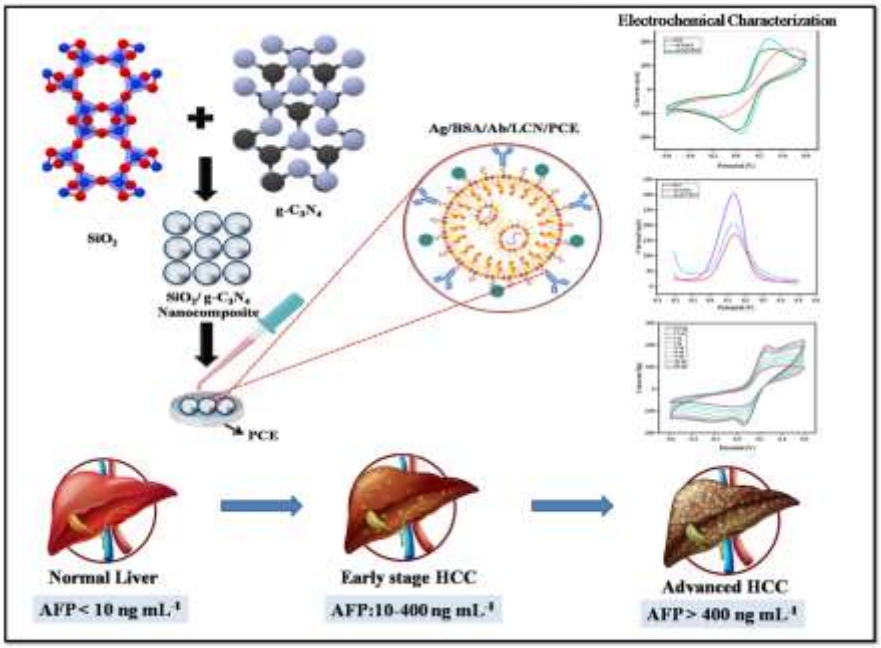

INTRODUCTION

Hepatocellular carcinoma (HCC) is still the most prevalent type of primary liver cancer and a serious global health concern [1]. According to the World Health Organisation (WHO) and the International Agency for Research on Cancer (IARC), liver cancer contributed 7.8% to the total number of cancer deaths in 2022 and is among the top three leading causes of cancer deaths [2]. In 2020, there were approximately 9,05,700 new cases and 8,03,200 deaths due to HCC globally, which clearly indicates the aggressive nature of the disease and poor survival rate [3]. In the future, WHO and IARC estimates indicate that the incidence and mortality rate of HCC will increase by more than 55% by 2040, with new cases and deaths estimated at 1.4 million and 1.3 million per year, respectively [4]. The high mortality rate of HCC patients is mainly due to the late diagnosis of the disease. Hence, there is an urgent need to develop diagnostic tools that are sensitive, rapid, and reliable for this type of cancer. Currently, the most used serum biomarker for screening HCC patients is alpha-fetoprotein

(AFP) [5]. However, its sensitivity relies on detecting small changes in its concentration levels, especially in the early stages of HCC development [6]. In healthy adults, the physiological level of this biomarker is about 10 ng/mL, while levels above 400 ng/mL are indicative of advanced-stage HCC development [7]. Therefore, identifying minor fluctuations in the levels of this biomarker is crucial for the early screening of HCC patients and for enhancing survival rates [8].
Despite this, traditional clinical methods of alpha-fetoprotein (AFP) detection, such as enzyme-linked immunosorbent assay (ELISA), radioimmunoassay (RIA), and radiological imaging, possess some limitations, which influence clinical practice [9,10]. For example, these traditional methods involve long periods of time and complicated procedures, which cause delays in diagnosis and put healthcare personnel under strain [11]. Moreover, these methods require specific and expensive devices and laboratories, which might restrict their application. Furthermore, these traditional methods might not possess the required level of sensitivity, speed, and simplicity, which are required for early diagnosis and point-of-care (POC) testing [12,13]. These limitations and drawbacks of traditional methods have, in turn, sparked considerable interest in electrochemical biosensing techniques, which possess high sensitivity, portability, low power consumption, and high signal transduction, thus making them suitable for POC testing [14]. Electrochemical biosensing techniques, therefore, have gained considerable attention and significance in the analysis of alpha-fetoprotein (AFP), due to their high analytical sensitivity, rapid signal processing, low power consumption, and ease of portability [15].
The transducer interface is the key component of an electrochemical biosensor and plays a crucial role in determining the analytical potential of the sensor, as the biological recognition process is accompanied by an electrical response [16]. For a biosensor signal to have a high degree of fidelity in the ultra-low concentration analysis of AFP, it is necessary to use a transducer with superior electron transfer rates, a high signal-to-noise ratio, and high stability, along with a suitable surface for antibody immobilization [17]. The employment of advanced nanomaterials may result in an improved charge transfer rate, increased electroactive surface area, and improved electrochemical response to achieve a detection limit that is significantly lower than that of existing methodologies [18,19]. Graphitic carbon nitride (g-C_3N_4) is a two-dimensional polymer that exhibits semiconductor properties and is primarily composed of nitrogen atoms. [20]. The material is a suitable candidate for a next-generation immunosensor platform owing to its good stability, suitable electronic properties, and compatibility with biorecognition elements [21,22]. However, the presence of strong nanosheet stacking and low conductivity are major disadvantages for g-C_3N_4. To address these issues, porous and biocompatible silicon dioxide (SiO_2) nanomaterials were integrated with g-C_3N_4 resulting in a hybrid material known for its elevated surface area and stability. The SCN hybrid material is likely to have a major impact on electron transfer rate, number of active binding sites, and establishment of a stable interface for biosensor development. In this study, a hybrid SCN nanocomposite material was synthesized and characterized for its physicochemical properties, followed by the development of an immunosensor for AFP detection.

MATERIALS AND METHODS

Chemicals and Reagents

Urea (≥99%), tetraethyl orthosilicate (TEOS, ≥98%), ammonia solution (25-28%), ethanol (≥99.5%), and phosphate-buffered saline (PBS, 0.01 M, pH 7.4) were bought from Merck (India). Alpha-fetoprotein (AFP) antigen (≥98% purity) and anti-AFP monoclonal antibodies (≥98.5% purity) were purchased from Sigma-Aldrich. The coupling agents that were employed in immobilization of the antibody were N-(3-Dimethylaminopropyl)-N7-ethylcarbodiimide hydrochloride (EDC, ≥98%) and N-hydroxysuccinimide (NHS, ≥98%). Electrochemical characterization studies were done using potassium ferricyanide/potassium ferrocyanide ($K_3[Fe(CN)_6]/K_4[Fe(CN)_6]$, 5mM, 1:1) redox electrolyte and potassium chloride (KCl). All solutions were made using ultrapure water (18.2 MΩ·cm). Analytical grade reagents were utilized, without any further purification.

Synthesis of g-C_3N_4

The bulk g-C_3N_4 was synthesized via the thermal polymerization of urea. Typically, 10 grams of urea were placed into a sealed alumina crucible and heated in a muffle furnace at a rate of 5°C per minute to reach 550°C, maintaining this temperature for 2 hours to ensure complete polymerization. Dried, white/yellowish g-C_3N_4 powders were obtained and stored for further use in the synthesis of nanocomposites [23,24].

Synthesis of SiO_2 Nanoparticles

A modified Stöber method was used to make SiO_2 nanoparticles. A mixture of 80 mL of ethanol and 10 mL of deionized water was prepared and stirred well under room temperature conditions. To this mixture, 5 mL of 25% ammonia solution was added, followed by the addition of 4 mL of TEOS with continuous stirring. The reaction mixture was allowed to react for 6 hours at room temperature, leading to the formation of uniform SiO_2 particles. The precipitate obtained was centrifuged, washed thrice with ethanol and deionized water, and finally dried at 60°C overnight. [25,26].

Preparation of SiO_2/g-C_3N_4 Nanocomposite

The SiO_2/g-C_3N_4 nanocomposite was synthesized using a standard method with an equal mass ratio of SiO_2 to g-C_3N_4 nanoparticles. Exactly 100 mg of g-C_3N_4 and 100 mg of SiO_2 nanoparticles were accurately measured and mixed in an agate mortar. To ensure a good mixture, 20 mL of ethanol was added. The mixture was ground for 20 minutes and then moved to a 50 mL beaker, where ultrasonication was performed to obtain a uniform nanoscale distribution of SiO_2 nanoparticles in the g-C_3N_4 matrix. The resulting mixture was then dried in a hot air oven at 60°C for 12 hours to evaporate the ethanol. After drying, the mixture was transferred to a crucible and subjected to thermal treatment at 450°C for 3 hours with a rate of 2°C/minute. After the mixture cooled down to room temperature, the SiO_2/g-C_3N_4 nanocomposite was obtained.

1. The synthesis of (a) SiO_2 NPs, (b) g-C_3N_4, and (c) SCN (SiO_2/g-C_3N_4) Nanocomposite

Fabrication of the SiO_2/g-C_3N_4 Modified Electrode

A paper-based electrode system (ItalSens IS-C series, PalmSens, The Netherlands) featuring three electrodes was utilized to fabricate an electrochemical immunosensor. The setup includes a carbon working electrode measuring 3 mm in diameter, a carbon counter electrode, and a built-in Ag/AgCl reference electrode. For the nanomodification of the electrode, 20 µL of SiO_2/g-C_3N_4 suspension (10 mg/mL in ethanol) was drop-casted onto the electrode and allowed to dry at room temperature. The modified electrode was thoroughly rinsed to get off the loosely bound material.

Activation and Antibody Immobilization

The amine ($–NH_2$) functionalities of g-C_3N_4 and hydroxyl (–OH) of SiO_2 on the nanocomposite surface were functionalized by EDC/NHS chemistry. A fresh solution of EDC/NHS in 1x PBS (pH 7.4) was used, and a 5 µL portion of the solution was added to the surface of the modified electrode and left overnight at 4°C to facilitate strong covalent binding [27]. Following this, the electrode was rinsed with PBS, and any unbound antibodies were blocked by incubating the electrode with bovine serum albumin (BSA, 1%) for 30 minutes [28]. This functionalized electrode, which incorporates the anti-AFP antibody, is designated as anti-AFP/SiO_2/g-C_3N_4.

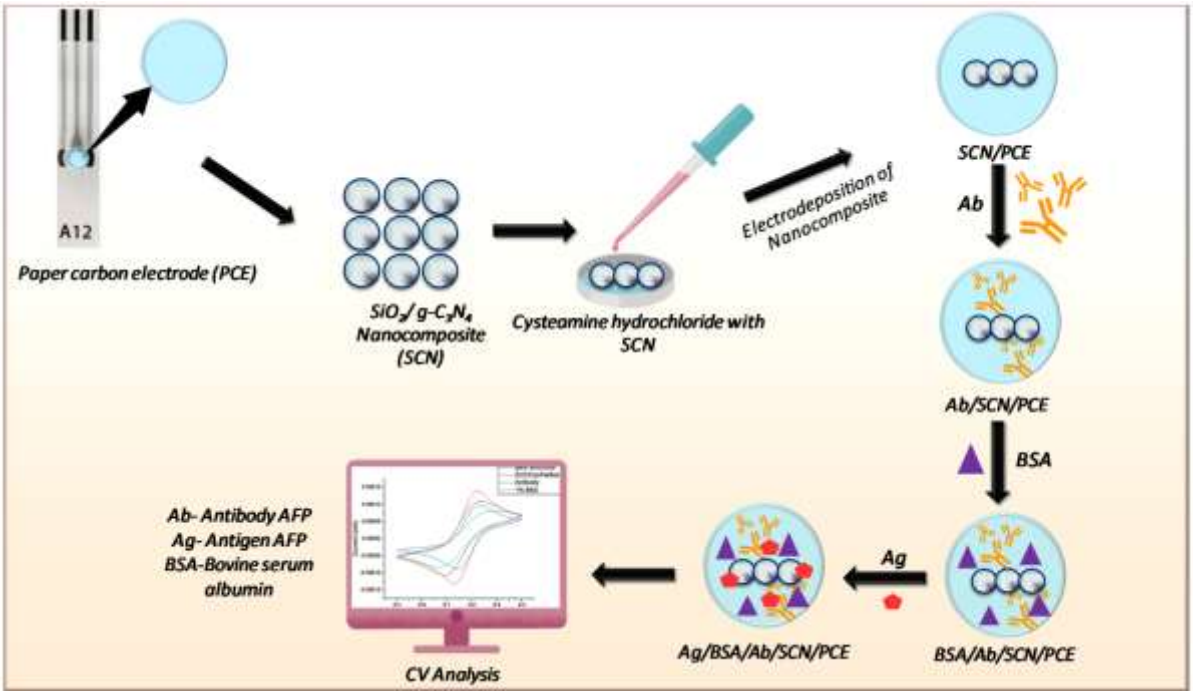

Figure 2. Schematic representation of the stepwise fabrication of the SCN (SiO_2/g-C_3N_4)-modified paper carbon electrode for AFP detection.

Electrochemical Measurements

The electrochemical experiments were carried out using a PalmSens4 Potentiostat/Galvanostat (Palmsens, Netherlands) and PSTrace software.

Cyclic Voltammetry (CV)

For cyclic voltammetry experiments, a 0.05 M KCl solution containing 5 mM of $[Fe(CN)_6]^{3-/4-}$ was utilized as the electrolyte. The potential sweep range extended from -0.6 V to +0.6 V with a scan rate of 50 mV/s.

Electrochemical Impedance Spectroscopy (EIS)

For the electrochemical impedance spectroscopy, a redox electrolyte of 5 mM $[Fe(CN)_6]^{3-/4-}$ was prepared in 0.05 M KCl, utilizing an amplitude of 10 mV and sweeping the frequency range from 0.1 Hz to 10^5 Hz.

Differential Pulse Voltammetry (DPV)

DPV was employed to assess AFP within an electrochemical range of -0.2 to +0.5V, utilizing a redox probe of 5 mM $[Fe(CN)_6]^{3-/4-}$ in a 0.05 M KCl solution. The technique measures changes in peak currents by monitoring DPV responses.

RESULTS

Characterization of synthesized nanoparticles

The synthesized nanomaterials were characterized using various physicochemical techniques to study their structural, functional, optical, and morphological properties. The methods used included X-ray Diffraction (XRD), Fourier Transform Infrared spectroscopy (FTIR), UV-Vis spectroscopy, Field-Emission Scanning Electron Microscopy (FESEM), and Energy-Dispersive Spectroscopy (EDS). The samples used were Silicon dioxide (SiO_2), graphitic-carbon nitride (g-C_3N_4), and the SCN (SiO_2/g-C_3N_4) nanocomposite. These methods were performed to confirm the successful synthesis of the samples, the compatibility of the composites, the purity of the phases, and the chemical interactions present.

Structural analysis (XRD)

X-ray diffraction analysis was employed to determine the crystalline structure, ordered phases, and stacking order of SiO_2, g-C_3N_4, and the SCN (SiO_2/g-C_3N_4) nanocomposite. The results showed a broad, low-intensity peak at $2\theta = 22°$, typical of amorphous silica, confirming the absence of crystallinity in the prepared SiO_2 [29,30]. The absence of sharp peaks indicates the absence of long-range periodic atomic ordering. The g-C_3N_4 sample showed two separate diffraction peaks corresponding to particular structural properties of graphitic carbon nitride: a low-angle diffraction peak at $2\theta = 13.11°$ for the (100) plane, indicating the regular arrangement of tri-s-triazine units in the plane [31,32], and a sharp peak at $2\theta = 27.5°$ for the (002) plane, indicating layered stacking of the aromatic units [33]. These peaks confirm the successful formation of a graphitic structure with maintained layering in g-C_3N_4. The SCN nanocomposite showed diffraction patterns confirming the coexistence of SiO_2 and g-C_3N_4. The major peak appeared at $2\theta = 27.5°$, indicating the stacking of g-C_3N_4 layers [34]. While the broader, amorphous SiO_2 diffraction peak was observed, it was not the major peak, indicating a high level of g-C_3N_4 integration into the SiO_2 matrix. The lower intensity of the broader amorphous SiO_2 diffraction peak compared to the strong g-C_3N_4 diffraction peak indicates good dispersion and potential interfacial interactions, which may be useful in promoting long-range order in the composite material.

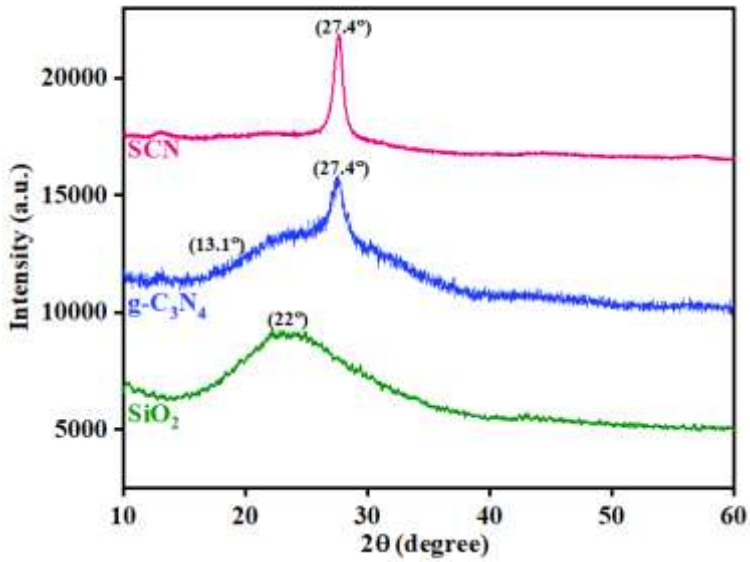

Figure 3(a) The X-ray diffraction (XRD) pattern of the SiO_2 NPs, g-C_3N_4, and SiO_2/g-C_3N_4 (SCN) nanocomposite.

Functional Group Analysis (FTIR)

FTIR spectroscopy was conducted for the analysis of chemical bonds, functional groups, and possible interactions between SiO_2 and g-C_3N_4 in the composite material. In the FTIR spectrum of SiO2 nanoparticles, the distinctive absorption peaks for the asymmetric and symmetric stretching of Si-O-Si bonds were observed at 1087 cm^{-1} and 810 cm^{-1}, respectively [35]. The prominent absorption peak around 3500 cm^{-1} is ascribed to the O-H stretching from either adsorbed water or the surface hydroxyl groups present on the silica [36]. The absorption bands of the triazine ring were found in the region of 1560, 1400, and 1300 cm^{-1} [37]. The vibrational modes of the triazine ring were found in the range of 810 cm^{-1} to 820 cm^{-1}. [38,39]. In the FTIR spectrum of the composite material, the intense absorption band is attributed to the N-H stretching of the surface hydroxyl groups or the adsorbed water molecules. The FTIR absorption bands of the g-C_3N_4 component were found to be of high intensity, confirming the presence of the component in the composite material. The shifts in the bands indicate the presence of certain interactions between the two components, possibly hydrogen bonds or electrostatic interactions between the hydroxyl groups of the silica and the nitrogen sites of the g-C_3N_4 component.

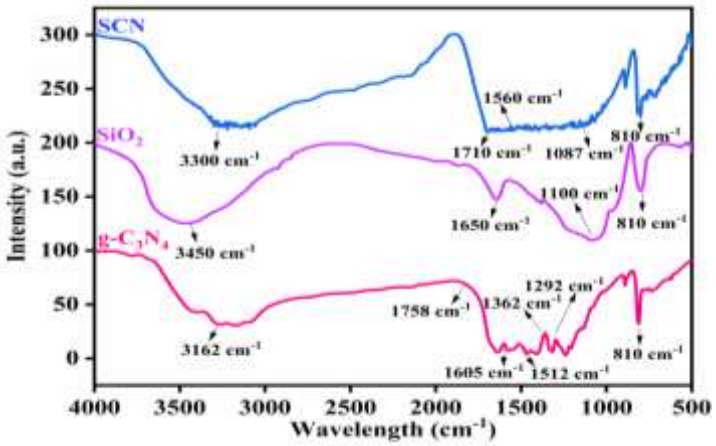

Figure 3(b) Fourier-transform infrared (FTIR) spectra of the SiO_2 NPs, g-C_3N_4, and SiO_2/g-C_3N_4 (SCN) nanocomposite.

Optical Properties (UV-Visible spectroscopy)

In order to investigate the electronic and optical properties of the synthesized nanomaterials, UV-visible absorption spectroscopy was used. The g-C_3N_4 nanomaterial exhibited two distinct absorption peaks. The distinct absorption edge observed at 450 nm is attributed to the π-π* transitions within the conjugated carbon nitride structure, whereas the second absorption peak at 350 nm is linked to the n-π* transitions of the lone pair electrons present on the nitrogen atoms [40,41]. On the other hand, the SiO_2 exhibited minimum absorption in the visible region due to the large bandgap energy of the material [42]. The absorption spectra of the SCN composite material exhibited the same general absorption profile as the g-C_3N_4 nanomaterial, but they shifted to the blue region and increased absorption in the UV region. This indicates the electronic interaction between the two materials, suggesting the band gap energy changes upon the incorporation of the SiO_2 material. This indicates the improved efficiency of the electron transfer process for the composite material.

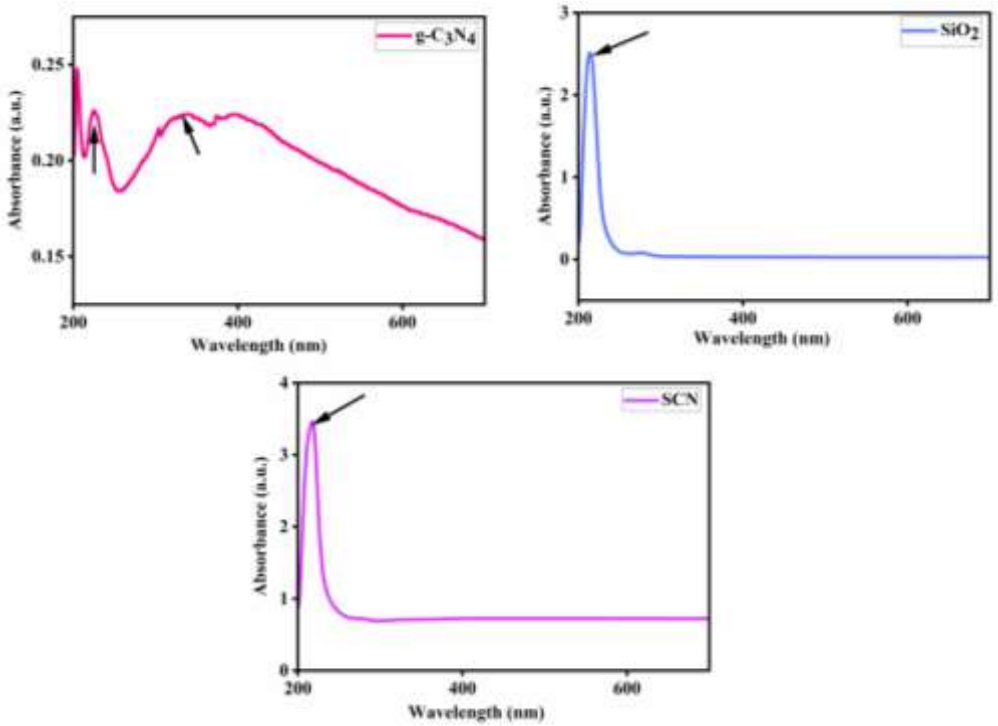

Figure 3(c) Ultraviolet-visible absorption spectra of the SiO_2 NPs, g-C_3N_4, and SiO_2/g-C_3N_4 (SCN) nanocomposite.

Morphological Analysis (FESEM)

FESEM was conducted to examine the surface morphology, particle arrangement, and the degree of structural integration in each sample [43]. The FESEM of SiO_2 reveals particles are irregularly shaped and clustered, which indicates the formation of amorphous silica. SiO_2 nanoparticles are porous and can easily form networks due to the large surface area, which makes them useful when they are incorporated into the nanocomposite material. In contrast, the FESEM of g-C_3N_4 shows that it is arranged in layers or sheets and has wrinkles and folds, indicating that it is partially exfoliated and has the natural tendency to form tri-s-triazine structures. The nanosheets were found to be porous and had a sharp structure. The SiO_2 nanoparticles are uniformly distributed on and between the g-C_3N_4 nanosheets in the SCN composite material. The structure combines a spherical silica cluster and a planar carbon nitride sheet. The uniform distribution of the SiO_2 nanoparticles suggests good interfacial bonding and a successful composite material.

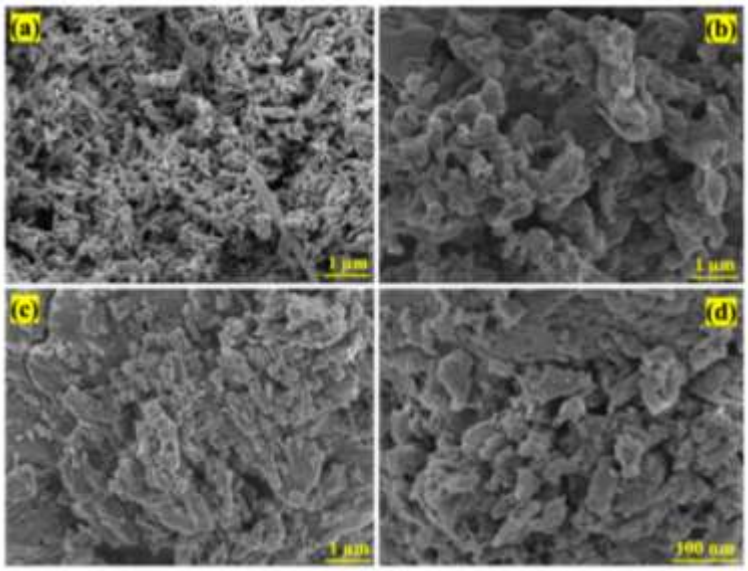

Figure 3(d) Field Emission Scanning Microscopy of (a) SiO_2 nanoparticles (×20.00k), (b) g-C_3N_4(×20.00k), (c) SCN nanocomposite (×20.00k), and SCN nanocomposite (×30.00k).

Elemental Composition (EDS)

The elemental composition was further confirmed by EDS, which showed successful integration of the elements in the composite, as evidenced by the presence of distinct peaks of Si and O. Moreover, there was no presence of impurity elements in the EDS spectra of SiO_2. The EDS spectra of g-C_3N_4 showed significant peaks of C and N, which corresponded to the ratio of carbon nitride polymers. The EDS spectra of SCN nanocomposite showed significant peaks of C, O, and N, which further confirms the coexistence of both materials in the composite. Elemental mapping further showed the homogenous distribution of Si and O of SiO_2 and the homogenous distribution of C and N of g-C_3N_4 [44]. This proves great homogeneity and integration of two different elements, where there was no presence of impurity and undesirable elements.

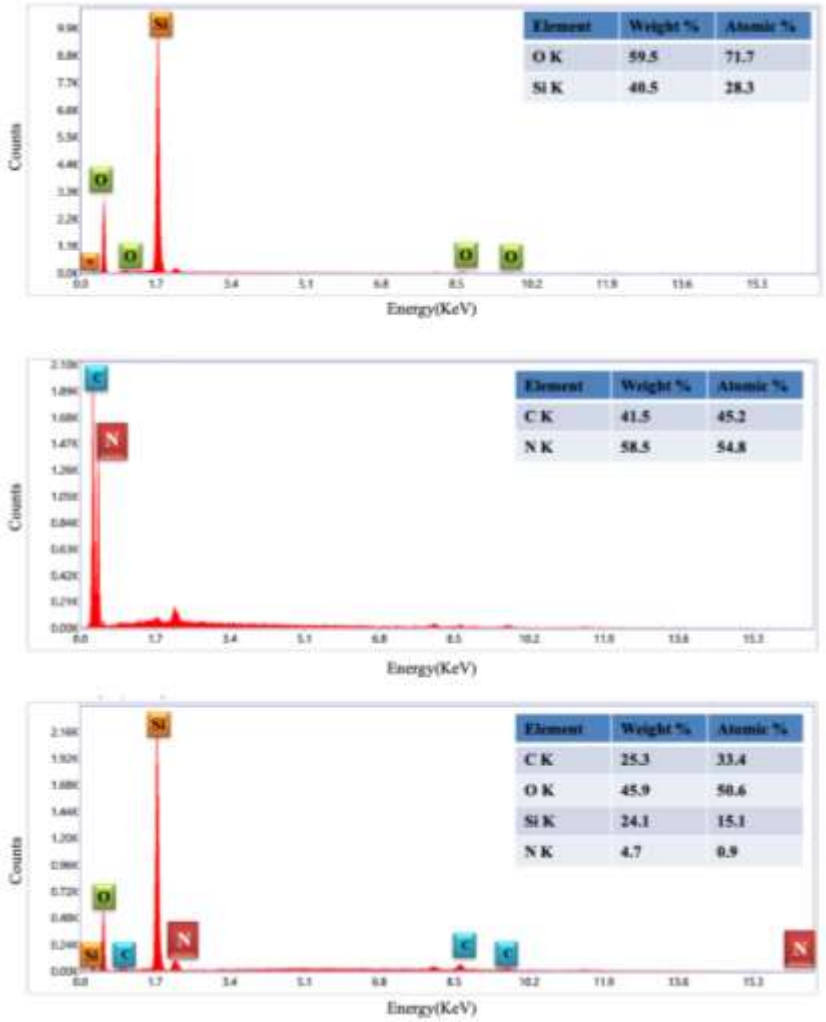

Figure 3(e) Energy-Dispersive X-ray Spectroscopy of SiO_2 nanoparticles, g-C_3N_4, and SCN (SiO_2/g-C_3N_4) nanocomposites.

Electrochemical characterization of the fabricated immunosensor

The PCE was systematically analyzed via CV, DPV, and EIS to investigate the impact of multiple electrochemical modifications on the electrode. All three techniques provide quantitative and/or qualitative information about interfacial electron transfer processes and changes in electrochemical and physical quantities on the electrode surface as a result of functionalization [45].

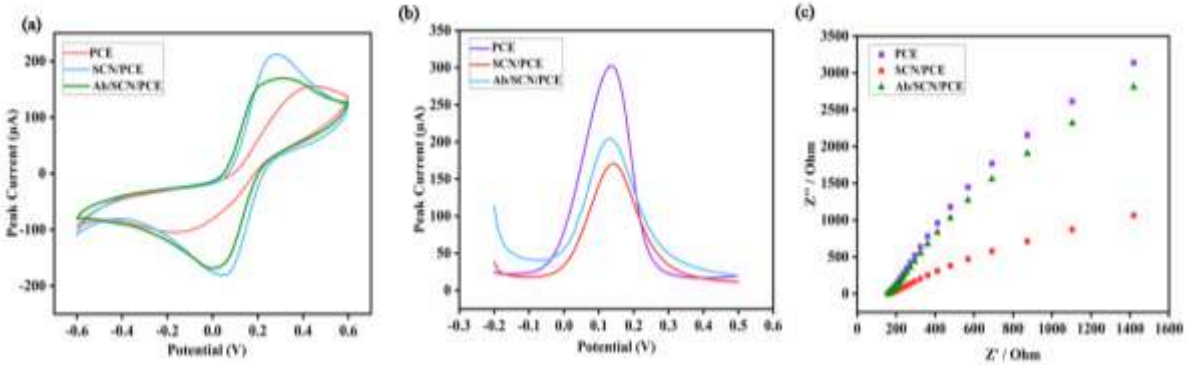

Figure 4(a-c) illustrates the electrochemical behavior of the bare paper carbon electrode (PCE), SCN-modified PCE (SCN/PCE), and antibody-functionalized electrode (Ab/SCN/PCE), as evaluated using cyclic voltammetry (CV), differential pulse voltammetry (DPV), and electrochemical impedance spectroscopy (EIS), respectively.

Cyclic Voltammetry Response of Bare and SCN-Modified Electrodes

In Figure 4(a), the bare PCE displayed quasi-reversible peaks during the redox reaction of $[Fe(CN)_6]^{3-/4-}$. This indicated a limited electroactive surface area (Ip = 155.2 μA) with a peak-to-peak separation of 0.44V, implying a moderate rate of electron transfer. When the SCN interacted with the PCE surface, both anodic and cathodic peak currents increased. This indicated improved electrical conductivity and a higher rate of electron transfer. The electrochemistry was significantly improved as shown in Figure 4(b), with an Ip of 212.34 μA and a peak-to-peak separation of 0.27V. The SCN nanostructure contributed to an increased surface area and enhanced the interfacial charge transfer between the electrode and the electrolyte solution. Upon the addition of the antibody to the surface (Ab/SCN/PCE), a reduction in the peak current was observed, as illustrated in Figure 4(c). The redox current was reduced to an Ip of 169.66 μA with a peak-to-

peak separation of 0.30V as a result of the steric and electrostatic effects of the antibody on the surface, which hindered the rate of electron transfer to a certain extent. The CV curve varied as expected, indicating that the surface modifications were successful and that the antibody was effectively immobilized on the surface of the PCE.

Electroactive Surface Area (EASA) Determination

The electrochemically active surface area (EASA) was determined based on the cyclic voltammetry data obtained for the system. The calculation was performed using the Randles-Sevcik equation for reversible electrochemical reactions. This equation was expressed by the formula $Ip = (2.69 \times 10^5)\, n^{3/2}\, A\, D^{1/2}\, C\, v^{1/2}$. Here, Ip represents the peak current amplitude, n is the number of electrons transferred in the electrochemical reactions (n=1), A is the electroactive surface area, and D is the diffusion coefficient of the electroactive material $[Fe(CN)_6]^{3-/4-}$, which was taken as (6.7×10^{-6} $cm^2\ s^{-1}$). The anodic peak currents were used to obtain the EASA values, which were found to be 0.188 cm^2 for bare PCE, 0.257 cm^2 for SCN/PCE, and 0.205 cm^2 for Ab/SCN/PCE.

The electrochemically active surface area showed significant changes upon the modification of the PCE electrode. Specifically, the EASA increased to 0.257 cm^2 upon the introduction of the SCN nanocomposite. This represented an enhancement of 36.7% compared to the value of 0.188 cm^2 for the bare PCE. This significant increase indicated successful formation of the electrochemical interface. This enhancement was attributed to the synergistic effects of the g-C_3N_4 nanosheets, while the SiO_2 nanoparticles increased the surface roughness, which in turn exposed a greater density of electroactive sites and also facilitated improved charge transfer kinetics [46].

Differential Pulse Voltammetry (DPV)

The results obtained in the cyclic voltammetry (CV) test were further validated by the differential pulse voltammetry (DPV) test results, as depicted in Fig. 4(b). For the SCN/PCE, a considerably higher peak current of 302.4 µA was observed compared to the bare PCE, which exhibited a peak current of 171.05 µA. In the Ab/SCN/PCE, a decreased current response of 204.8 µA was observed, which is consistent with the formation of a bioactive and electrically resistive antibody film. The substantial differences in the observed peak current values among the PCE, SCN/PCE, and Ab/SCN/PCE indicated the strong potential of the differential pulse voltammetry technique for the detection of biomolecules.

Electrochemical Impedance Spectroscopy and Nyquist Plot Analysis

Electrochemical impedance spectroscopy (EIS) was used to study the charge transfer kinetics at the interface [47]. As shown in Figure 4(c), there were large variations in the charge transfer resistance (Rct = 946.9 Ω) during the modification process, as indicated by the variations in the Nyquist plots. The unmodified PCE exhibited a relatively large semicircular diameter in the EIS spectrum, corresponding to an Rct value of 946.9 Ω, indicating poor electron transfer kinetics. After modification with the SCN film, the diameter of the semicircle portion was significantly reduced, yielding a charge transfer resistance (Rct) of approximately 534.4 Ω. This suggested that the interfacial resistance was decreased and the charge transfer efficiency was enhanced due to the presence of the conductive nanostructured film. After the immobilization of antibodies onto the PCE surface, a significant increase in Rct (715.9 Ω) was observed, as indicated by the enlarged semicircular diameter in the EIS spectrum of the Ab/SCN/PCE. This phenomenon was attributed to the formation of a bio-insulating interface, which hindered the electron transfer rate at the interface between the electrode surface and the redox electrolyte [48].

Exchange Current Density and Electron-Transfer Rate Constant

The exchange current density (i_0) was calculated using the equation: $i_0 = \frac{RT}{nFRct}$. In addition, the i_0 values increased from 2.7×10^{-5} A for the unmodified PCE to 4.8×10^{-5} A for the SCN-modified electrode. This indicated a nearly two-fold enhancement in the efficiency of the redox process. The heterogeneous electron transfer rate constant (k_0) was calculated using the equation $k_0 = \frac{i0}{nFAC}$. The concentration (C) was taken as 5.0 mM. As a result, the k_0 value increased from 7.9×10^{-4} cm s^{-1} to 1.4×10^{-3} cm s^{-1}, which suggested an acceleration of the interfacial electron transfer process in the SCN-modified electrode. Overall, the results obtained from cyclic voltammetry (CV), differential pulse voltammetry (DPV), and electrochemical impedance spectroscopy (EIS) provided strong evidence for the successful and stepwise development of the SCN-based electrochemical immunosensor. In summary, the SCN film significantly enhanced the electrochemical properties of the PCE, while the immobilization of the antibody introduced measurable resistance changes, which were critical for the development of the immunosensor. In addition, the electrochemical transitions were well defined during each step of the modification, which demonstrated the reliability and efficiency of the developed immunosensor.

Immunosensor performance analysis

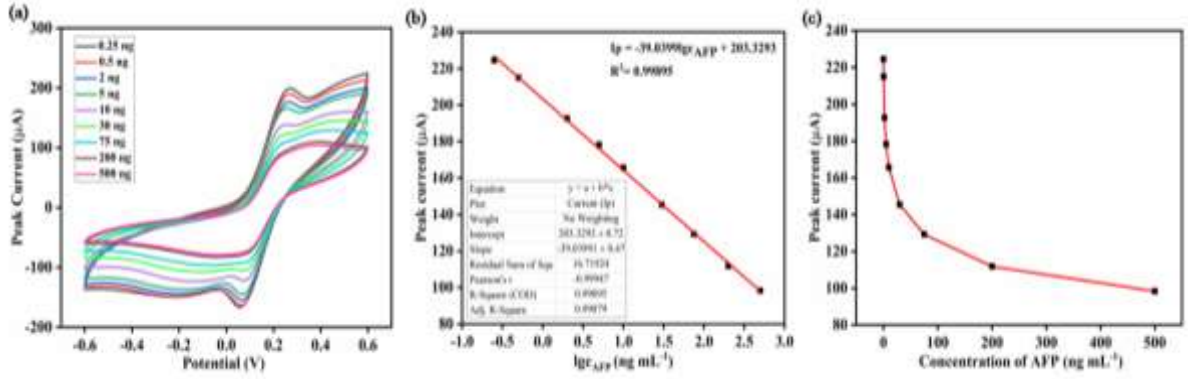

Figure 5(a) Cyclic voltammograms of the Ab/SCN/PCE immunosensor were recorded in 5 mM $[Fe(CN)_6]^{3-/4-}$ with 0.05 M KCl at a scan rate of 50 mV s^{-1}, showing results with increasing concentrations of antigen (ranging from 0.25 to 500 ng mL^{-1}), (b) The corresponding change in anodic peak current (Ip) is plotted against antigen concentration, revealing a steady decline in current response as antigen levels increase, and (c) Calibration plot of anodic peak current (Ip) against the logarithm of antigen concentration (log C), demonstrating a linear correlation within the concentration range.

Figure 5(a) shows the cyclic voltammogram (CV) of the developed immunosensor for different concentrations of antigen ranging from 0.25 to 500 ng/mL. A significant decrease in the anodic peak current (Ip) was noticed with the increase in antigen concentration, confirming the successful formation of the antigen-antibody immunocomplex film on the electrode surface. The film acts as an impediment to electron transfer reactions, thus reducing the current [49].
Figure 5(b) illustrates the variation of peak current (Ip) with antigen concentration. The significant decrease in Ip at lower concentrations indicates the high sensitivity of the biosensor, while the reduced sensitivity at higher concentrations indicates the saturation of active binding sites. Moreover, the data show the high repeatability of the biosensor, as indicated by the negligible variation in the response signal.
The performance analysis was studied using a calibration plot where Ip was plotted against the logarithmic value of the antigen concentration, as shown in Figure 5(c). The plot shows a strong linear relationship between Ip and Log C, with the regression equation given by Ip = 203.33 – 39.03 log C. In this equation, Ip is the peak current in microamperes, and C is the antigen concentration in ng mL^{-1}. The analysis of the calibration plot gives a y-intercept value of 203.33 ± 0.72 and a slope value of -39.03 ± 0.48. The linearity of the plot was further confirmed by the high correlation coefficient (r) value of 0.998 and the coefficient of determination (R^2) of 0.998, which shows a high degree of accuracy in the quantitative analysis of the system. Moreover, the Pearson correlation coefficient of -0.999 reveals the relationship between the peak current and the antigen concentration, which shows a strong inverse proportionality. This phenomenon can be explained by the surface blocking effect caused by the formation of antigen-antibody complexes, as mentioned in the previous section. Due to the high linearity and correlation coefficient, the limit of detection (LOD) and limit of quantification (LOQ) of the system were calculated using the standard formulas LOD = $\frac{3\sigma}{S}$ and LOQ = $\frac{10\,\sigma}{S}$, where σ represents the standard deviation of blank signal, and S represents the slope of the regression equation (39.03 μA $\log^{-1}$ ng mL^{-1}). Consequently, the LOD and LOQ of the system were determined to be 0.00224 ng mL^{-1} and 0.00679 ng mL^{-1}, respectively, which demonstrated the high sensitivity of the developed electrochemical biosensor for the detection of critical cancer biomarkers.

Optimization and evaluation of experimental conditions

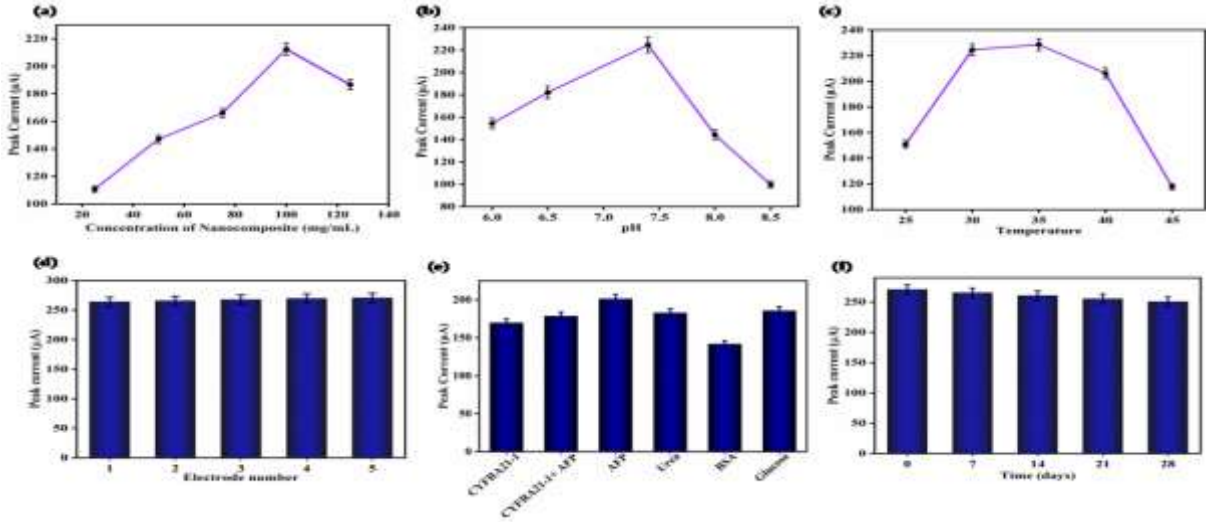

Figure 6 (a–f) illustrates the optimization of key experimental parameters influencing the electrochemical response of the SCN/PCE-based electrochemical sensor. (a) Impact of nanocomposite concentration (ng mL^{-1}) on the peak current response, (b) Effect of pH solution on the electrochemical peak current, (c) Influence of operating temperature on the performance of the sensor, (d) Evaluation of reproducibility showing current response across five consecutive trials, (e) Selectivity assessment of the sensor in the presence of potential interfering substances compared to the target analyte, and

(f) Evaluation of the stability of the fabricated electrodes over a storage period of 28 days. Error bars indicate the standard deviation from three measurements.

The effect of nanocomposite concentration was also investigated in the range of 25-125 ng mL^{-1}, and the results are shown in Figure 6(a). As the nanocomposite concentration increased, the peak current also increased to reach 100 ng mL^{-1}. This is attributed to the increased electrical conductivity of the nanocomposite material, where higher concentrations provide a higher number of electroactive sites, thus increasing the peak current. However, concentrations above 100 ng mL^{-1} caused a decrease in the peak current, which may be due to the aggregation of nanomaterials on the electrode surface, thus reducing the electroactive area. All experiments were done in triplicate, as shown in Figure 6(a). One-way analysis of variance (ANOVA) was used to determine the significance of differences in the peak currents among the various nanocomposite concentrations, and the results showed significant differences ($p < 0.01$).
The pH-biosensor response relationship, as shown in Figure 6(b), clearly shows that the peak current increases from 155 µA at pH 6.0 to 225 µA at pH 7.4, followed by a drastic decrease at higher pH values. In addition, one-way ANOVA shows that pH has a significant effect on the current response at a significance level of less than 0.01. The higher peak current measured at pH 7.4 is due to the optimal antigen-antibody reaction, faster electron transfer rates, and the conductivity of the SCN-modified electrode surface at near-physiological pH values as a result of surface deprotonation. However, the peak current decreases drastically at higher pH values, reaching 145 µA at pH 8.0 and 100 µA at pH 8.5. The optimum pH value for electrochemical analysis was found to be 7.4, which ensures maximum sensitivity and stability of the output response.
Figure 6(c) shows the effect of temperature on the biosensor signal, which clearly shows a strong correlation between the peak current and temperature. With the increase in temperature from 25 to 35°C, the peak current increase significantly from 150 to 230 µA. This is because of the increased kinetics of charge transfer and increased mass transport at the electrode/electrolyte interface, which result in more efficient antigen-antibody interactions. The peak current at 35°C shows the optimal reaction conditions. After 35°C, the peak current drops significantly to 205 µA at 40°C and 120 µA at 45°C due to biomolecular denaturation at higher temperatures. Therefore, 35°C was chosen as optimal temperature for subsequent electrochemical analysis.
The reproducibility of the fabricated immunosensor was evaluated by carrying out five successive measurements under the same conditions (Figure 6(d)). The data showed constant peak current values with an average of 268 µA and very small differences among the measurements. The standard deviation was between 4 and 6 µA, with a relative standard deviation (RSD) of 1.7%. The above results clearly show that the SCN-modified electrode has a high reproducibility in charge transfer and biomolecular adhesion.

The selectivity of the designed biosensor for the detection of alpha-fetoprotein (AFP) was tested by observing the peak current value in the presence of possible interfering agents, as shown in Figure 6(e). The biosensor showed a significantly higher response to AFP, reaching a maximum peak current of about 200 µA, compared to common interferents such as urea, glucose, and BSA. In particular, the current response due to AFP was found to be higher than that of non-specific molecules by about 20-30%. This small standard deviations in this experiment (error bars < 5% of the mean current) further confirm the statistical validity of the results. These results confirm high selectivity and anti-interference ability, which can be attributed to the specific antigen-antibody reaction and the surface properties of the SCN-modified electrode.
The stability of the biosensor was tested for a period of 28 days, as shown in Figure 6(f). Cyclic voltammetry (CV) analysis of the immunosensor was performed on Days 1, 7, 14, 21, and 28, using an AFP antigen concentration of 10 ng mL^{-1}. After the analysis, the immunosensor was stored in the refrigerator at 4°C. The decrease in the peak current response was found to be 2.00%, 3.70%, 5.70%, and 7.40% on Days 7, 14, 21, and 28, respectively. As a result, the immunosensor retrained 92.6% of its original current response after 28 days. The decrease in the peak current from 270.365 µA on Day 1 to 250.358 µA on Day 28 was found to be a modest change of 7.40%, indicating good storage stability of the biosensor. The low values of relative standard deviation, appropriate sample size, and statistically significant ANOVA results further confirm the robustness, validity, and analytical ability of the fabricated biosensor, thus establishing its high applicability for the detection of cancer biomarkers.

Table 1. Comparative evaluation of electrochemical immunosensors using nanomaterials for the detection of AFP.

Immunosensor platform	Linear range (ng mL^{-1})	Limit of detection (ng mL^{-1})	References
AuNPs/PGNR	5-60	1	[50]
Au/AET/PAMAM	5-500	3	[51]
Fe_3O_4@AuNPs	1-200	0.65	[52]
Thionine-AuNPs	0.05-100	0.012	[53]
HRP-MPS/PVA/ITO	1-90	0.5	[54]
Self-assembled monolayers AuNPs/HRP	15-350	5	[55]
SiO_2/g-C_3N_4	**0.25-500**	**0.00224 ng/mL**	**Present work**

Clinical translation challenges and prospects
The electrochemical biosensor, as described in this study, has shown promising analytical characteristics in a controlled environment. However, there are certain issues to be addressed to translate this device into a clinical tool. The first issue to be addressed is to evaluate the device's analytical performance in a complex clinical matrix, such as serum or plasma. This is because there are certain issues to be taken into account in a clinical environment, such as nonspecific binding and

biomolecular interactions. Another problem that needs to be addressed is the ability to prove the manufacturability of the device on a large scale and with consistent analytical performance. It is also important to address the long-term stability of the biorecognition components and the development of surface chemistries that are amenable to mass production. Another important domain for future research work is the standardization of sample preparation methods and their efficient integration with user friendly devices for effective POC testing. It is recommended that clinical validations be performed on large scale using patient samples in future studies. The use of microfluidic technology for automating low value SA and their integration with portable electronic devices for real-time data acquisition is also recommended in future studies.

CONCLUSIONS

This research work presents the successful fabrication of a highly sensitive electrochemical immunosensor based on SCN heterostructure, in which the charge transfer rate at the electrode interface is significantly improved by taking advantage of the unique electronic properties of the nanocomposite material. The immunosensor was fabricated for the quantitative determination of the liver cancer biomarker alpha-fetoprotein (AFP), thus offering a trustworthy analytical tool for the early diagnosis of the liver cancer. This is evidenced by the detection sensitivity of 0.00224 ng mL^{-1}. Moreover, the immunosensor showed a remarkable architectural stability, retaining 92.6% of its biological activity after 28 days, indicating potential applicability for the early diagnosis of hepatocellular carcinoma (HCC). Additionally, the high analytical accuracy of the immunosensor was confirmed by its low relative standard deviation of 1.7%, thus ensuring the reliable and accurate acquisition of data. Therefore, the immunosensor developed in this research work offers a stable, sensitive, and cost-effective analytical tool for the early diagnosis of HCC.

Declaration of Conflict Interest

The authors declare that there is no known conflict of interest or personal relationships that could have appeared to influence the work reported in this paper.

Funding

Ms. Samiksha acknowledges financial support from the Council of Scientific and Industrial Research (CSIR), Government of India, under the Junior Research Fellowship (JRF) scheme (File No. 09/1063(20596)/2024-EMR-I; Ref. No: Dec-23 (i)/EU-V).

Acknowledgement

The author sincerely thanks Ms. Damini Dahiya, PhD Research Scholar, Department of CEEES, Deenbandhu Chhotu Ram University of Science and Technology (Murthal, Haryana), for her valuable assistance in figure preparation, illustration, and for her critical review of the manuscript.

REFERENCES

[1] Rumgay, H., Arnold, M., Ferlay, J., Lesi, O., Cabasag, C. J., Vignat, J., and Soerjomataram, I. 2022. Global burden of primary liver cancer in 2020 and predictions to 2040. *Journal of hepatology*, *77*(6): 1598-1606. https://doi.org/10.1016/j.jhep.2022.08.021.

[2] Mattiuzzi, C., and Lippi, G. 2020. Cancer statistics: a comparison between world health organization (WHO) and global burden of disease (GBD). *European journal of public health*, *30*(5): 1026-1027. https://doi.org/10.1093/eurpub/ckz216.

[3] Lazzaro, A., and Hartshorn, K. L. 2023. A comprehensive narrative review on the history, current landscape, and future directions of hepatocellular carcinoma (HCC) systemic therapy. *Cancers*, *15*(9): 2506. https://doi.org/10.3390/cancers15092506.

[4] Bertuccio, P., Turati, F., Carioli, G., Rodriguez, T., La Vecchia, C., Malvezzi, M., and Negri, E. 2017. Global trends and predictions in hepatocellular carcinoma mortality. *Journal of hepatology*, *67*(2): 302-309. https://doi.org/10.1016/j.jhep.2017.03.011.

[5] Wei, Z., Zhang, Y., Lu, H., Ying, J., Zhao, H., and Cai, J. 2022. Serum alpha-fetoprotein as a predictive biomarker for tissue alpha-fetoprotein status and prognosis in patients with hepatocellular carcinoma. *Translational Cancer Research*, *11*(4): 669. https://doi.org/10.2103/tcr-21-2334.

[6] Ayuso, C., Rimola, J., Vilana, R., Burrel, M., Darnell, A., García-Criado, Á., and Brú, C. 2018. Diagnosis and staging of hepatocellular carcinoma (HCC): current guidelines. *European journal of radiology*, *101*, 72-81. https://doi.org/10.1016/j.ejrad.2018.01.025.

[7] Sengupta, S., and Parikh, N. D. 2017. Biomarker development for hepatocellular carcinoma early detection: current and future perspectives. *Hepatic oncology*, *4*(4): 111-122. https://doi.org/10.2217/hep-2017-0019.

[8] Piñero, F., Dirchwolf, M., and Pessôa, M. G. 2020. Biomarkers in hepatocellular carcinoma: diagnosis, prognosis, and treatment response assessment. *Cells*, *9*(6): 1370. https://doi.org/10.3390/cells9061370.

[9] Niaki, N. M., Hatefnia, F., Heidari, M. M., Tabean, M., and Mobed, A. 2025. Alpha-fetoprotein (AFP) biosensors. *Clinica Chimica Acta*, *573*, 120293. https://doi.org/10.1016/j.cca.2025.120293.

[10] Ramachandran, L., Abul Rub, F., Hajja, A., Alodhaibi, I., Arai, M., Alfuwais, M., and Mani, N. K. 2024. Biosensing of alpha-fetoprotein: A key direction toward the early detection and management of hepatocellular carcinoma. *Biosensors*, *14*(5): 235. https://doi.org/10.3390/bios14050235.

[11] Debruyne, E. N., and Delanghe, J. R. 2008. Diagnosing and monitoring hepatocellular carcinoma with alpha-fetoprotein: new aspects and applications. *Clinica chimica acta*, *395*(1-2): 19-26. https://doi.org/10.1016/j.cca.2008.05.010.

[12] Yang, S. M., Lv, S., Zhang, W., & Cui, Y. 2022. Microfluidic point-of-care (POC) devices in early diagnosis: A review of opportunities and challenges. *Sensors*, *22*(4): 1620. https://doi.org/10.3390/s22041620.

[13] Heidt, B., Siqueira, W. F., Eersels, K., Diliën, H., van Grinsven, B., Fujiwara, R. T., and Cleij, T. J. 2020. Point of care diagnostics in resource-limited settings: a review of the present and future of PoC in its most needed environment. *Biosensors*, *10*(10): 133. https://doi.org/10.3390/bios10100133.
[14] da Silva, E. T., Souto, D. E., Barragan, J. T., de F. Giarola, J., de Moraes, A. C., and Kubota, L. T. 2017. Electrochemical biosensors in point-of-care devices: recent advances and future trends. *ChemElectroChem*, *4*(4): 778-794. https://doi.org/10.1002/celc.201600758.
[15] Amarnath, C. A., and Sawant, S. N. 2020. Polyaniline-based electrochemical biosensor for α-fetoprotein detection using bio-functionalized nanoparticles as a detection probe. *Electroanalysis*, *32*(11): 2415-2421. https://doi.org/10.1002/elan.202060219.
[16] Grieshaber, D., MacKenzie, R., Vörös, J., and Reimhult, E. 2008. Electrochemical biosensors: sensor principles and architectures. *Sensors*, *8*(3): 1400-1458. https://doi.org/10.3390/s80314000.
[17] Nadeem-Tariq, A., Rafanan, J. R., Kang, N., Zhang, S., Kanniyappan, H., and Merchant, A. 2026. Electrochemical Detection of Cancer Biomarkers: From Molecular Sensing to Clinical Translation. *Biosensors*, *16*(1):44. https://doi.org/10.3390/bios16010044.
[18] Paul, R., Zhai, Q., Roy, A. K., and Dai, L. 2022. Charge transfer of carbon nanomaterials for efficient metal-free electrocatalysis. *Interdisciplinary Materials*, *1*(1): 28-50.https://doi.org/10.1002/idm2.12010.
[19] Baig, N., Sajid, M., and Saleh, T. A. 2019. Recent trends in nanomaterial-modified electrodes for electroanalytical applications. *TrAC Trends in Analytical Chemistry*, *111*, 47-61.https://doi.org/10.1016/j.trac.2018.11.044.
[20] Ong, W. J., Tan, L. L., Ng, Y. H., Yong, S. T., and Chai, S. P. 2016. Graphitic carbon nitride (g-C_3N_4)-based photocatalysts for artificial photosynthesis and environmental remediation: are we a step closer to achieving sustainability? *Chemical reviews*, *116*(12): 7159-7329. https://doi.org/10.1021/acs.chemrev.6b00075.
[21] Ramoso, J. P., Rasekh, M., and Balachandran, W. 2025. Graphene-based biosensors: Enabling the next generation of diagnostic technologies—A review. *Biosensors*, *15*(9): 586. https://doi.org/10.3390/bios15090586.
[22] Morawska, K., Sikora, T., Grabka, M., Wiśnik-Sawka, M., and Witkiewicz, Z. 2025. Early detection of threat agents: a review of bioimmunosensors and their prospects. *Critical Reviews in Analytical Chemistry*, 1-15. https://doi.org/10.1080/10408347.2025.2507346.
[23] Ge, L. 2011. Synthesis and photocatalytic performance of novel metal-free g-C_3N_4 photocatalysts. Materials Letters, 65(17-18): 2652-2654. https://doi.org/10.1016/j.matlet.2011.05.069.
[24] Chen, Z., Zhang, S., Liu, Y., Alharbi, N. S., Rabah, S. O., Wang, S., and Wang, X. 2020. Synthesis and fabrication of g-C_3N_4-based materials and their application in the elimination of pollutants. *Science of the Total Environment*, *731*, 139054. https://doi.org/10.1016/j.scitotenv.2020.139054
[25] Kim, Y. H., Lee, D. K., and Kang, Y. S. 2005. Synthesis and characterization of Ag and Ag–SiO_2 nanoparticles. *Colloids and Surfaces A: Physicochemical and Engineering Aspects*, *257*, 273-276.https://doi.org/10.1016/j.colsurfa.2004.07.035.
[26] Guo, Q., Huang, D., Kou, X., Cao, W., Li, L., Ge, L., and Li, J. 2017. Synthesis of disperse amorphous SiO_2 nanoparticles via sol–gel process. *Ceramics International*, *43*(1): 192-196.
https://doi.org/10.1016/j.ceramint.2016.09.133.
[27] Stanković, V., Đurđić, S., Ognjanović, M., Antić, B., Kalcher, K., Mutić, J., and Stanković, D. M. 2020. Anti-human albumin monoclonal antibody immobilized on EDC-NHS functionalized carboxylic graphene/AuNPs composite as promising electrochemical HSA immunosensor. *Journal of Electroanalytical Chemistry*, *860*, 113928.https://doi.org/10.1016/j.jelechem.2020.113928.
[28] Moulton, S. E., Barisci, J. N., Bath, A., Stella, R., and Wallace, G. G. 2003. Investigation of protein adsorption and electrochemical behavior at a gold electrode. *Journal of colloid and interface science*, *261*(2): 312-319.
https://doi.org/10.1016/S0021-9797(03)00073-0.
[29] Nazari, A., and Riahi, S. 2010. Microstructural, thermal, physical and mechanical behavior of the self-compacting concrete containing SiO_2 nanoparticles. *Materials Science and Engineering: A*, *527*(29-30), 7663-7672.
https://doi.org/10.1016/j.msea.2010.08.095.
[30] Yao, Y., Zhang, J., Xue, L., Huang, T., and Yu, A. 2011. Carbon-coated SiO_2 nanoparticles as anode material for lithium-ion batteries. *Journal of Power Sources*, *196*(23):10240-10243.https://doi.org/10.1016/j.jpowsour.2011.08.009.
[31] Alonso, A. V., Murugesan, A., Gogoi, R., Chandrabose, S., Abass, K. S., Sharma, V., and Kandhavelu, M. 2025. Graphitic carbon nitride nanoparticle: g-C_3N_4 synthesis, characterization, and its biological activity against glioblastoma. *European Journal of Pharmacology*, 177999.https://doi.org/10.1016/j.ejphar.2025.177999.
[32] Akintunde, O. O., Hu, J., Kibria, M. G., Pogosian, S., and Achari, G. 2023. A facile synthesis process of GCN/ZnO–Cu nanocomposite and the evaluation of the performance for the photocatalytic degradation of organic pollutants and the disinfection of wastewater under visible light. *Chemosphere*, *344*, 140287.
https://doi.org/10.1016/j.chemosphere.2023.140287.
[33] Warda, A. H., Rostom, M., Mashaly, M. I., Helmy, E. T., Gomaa, E. A., and AbouElleef, E. M. 2025. Facile and eco-friendly synthesis of GCN/ZnO nanocomposites for enhanced photocatalytic, antimicrobial, and antioxidant activities: applications in biomedicine and wastewater treatment. *Surfaces and Interfaces*, *72*, 107123.
https://doi.org/10.1016/j.surfin.2025.107123.
[34] Subashini, A., Prasath, P. V., Sagadevan, S., Lett, J. A., Fatimah, I., Mohammad, F., and Oh, W. C. 2021. Enhanced photocatalytic degradation efficiency of graphitic carbon nitride-loaded CeO_2 nanoparticles. *Chemical Physics Letters*, *769*, 138441.https://doi.org/10.1016/j.cplett.2021.138441.
[35] Nariyal, R. K., Kothari, P., and Bisht, B. 2014. FTIR measurements of SiO_2 glass prepared by the sol-gel technique. *Chemical Science Transactions*, *3*(3): 1064-1066. https://doi.org/10.7598/cst2014.816.
[36] Haque, F. Z., Nandanwar, R., Singh, P., Dharavath, K., and Syed, F. F. 2018. Effect of different acids and solvents on optical properties of SiO_2 nanoparticles prepared by the sol-gel process. *Silicon*, *10*(2), 413-419. https://doi.org/10.1007/s12633-016-9464-2.

[37] Araújo, J. C., Ferreira, D. P., Teixeira, P., and Fangueiro, R. 2021. In-situ synthesis of CaO and SiO_2 nanoparticles onto jute fabrics: exploring the multifunctionality. *Cellulose*, *28*(2): 1123-1138. https://doi.org/10.1007/s10570-020-03564-1.
[38] Xia, Y., Zhang, N., Zhou, Z., Chen, C., Wu, Y., Zhong, F., and He, Y. 2020. Incorporating SiO_2 functionalized g-C_3N_4 sheets to enhance anticorrosion performance of waterborne epoxy. *Progress in Organic Coatings*, *147*, 105768. https://doi.org/10.1016/J.PORGCOAT.2020.105768.
[39] Liu, J., Zou, R., Zhang, H., Song, Y., Liu, Y., Yang, S., and Peng, X. 2024. Enhanced π-electron transport in graphitic carbon nitride (g-C_3N_4) by constructing biochar-welded donor-acceptor (DA) configuration for photocatalytic conversion of biomass. *Applied Catalysis B: Environment and Energy*, *357*, 124312. https://doi.org/10.1016/J.APCATB.2024.124312.
[40] Anastasescu, C., Zaharescu, M., Angelescu, D., Munteanu, C., Bratan, V., Spataru, T., and Balint, I. 2017. Defect-related light absorption, photoluminiscence and photocatalytic activity of SiO_2 with tubular morphology. *Solar Energy Materials and Solar Cells*, *159*, 325-335. https://doi.org/10.1016/J.SOLMAT.2016.09.032.
[41] Liang, Q., Liu, X., Wang, J., Liu, Y., Liu, Z., Tang, L., and Feng, C. 2021. In-situ self-assembly construction of hollow tubular g-C_3N_4 isotype heterojunction for enhanced visible-light photocatalysis: experiments and theories. *Journal of hazardous materials*, *401*, 123355. https://doi.org/10.1016/J.JHAZMAT.2020.123355.
[42] Li, F., Huang, X., Jiang, Y., Liu, L., and Li, Z. 2009. Synthesis and characterization of ZnO/SiO_2 core/shell nanocomposites and hollow SiO_2 nanostructures. *Materials Research Bulletin*, *44*(2), 437-441. https://doi.org/10.1016/J.MATERRESBULL.2008.04.024.
[43] Boonprakob, N., Wetchakun, N., Phanichphant, S., Waxler, D., Sherrell, P., Nattestad, A., and Inceesungvorn, B. 2014. Enhanced visible-light photocatalytic activity of g-C_3N_4/TiO_2 films. *Journal of colloid and interface science*, *417*, 402-409. https://doi.org/10.1016/J.JCIS.2013.11.072.
[44] Boonprakob, N., Wetchakun, N., Phanichphant, S., Waxler, D., Sherrell, P., Nattestad, A., and Inceesungvorn, B. 2014. Enhanced visible-light photocatalytic activity of g-C_3N_4/TiO_2 films. *Journal of colloid and interface science*, *417*, 402-409. https://doi.org/10.1016/J.ARABJC.2019.07.009.
[45] Chen, X., Sun, Y. L., Lin, X. M., Dong, J. C., and Li, J. F. 2026. In situ Studies of Electrochemical Energy Conversion and Storage Technologies: From Materials, Intermediates, and Products to Surroundings. *Nano-Micro Letters*, *18*(1), 170. https://doi.org/10.1007/s40820-025-02014-6.
[46] Lin, B., Xue, C., Yan, X., Yang, G., Yang, G., and Yang, B. 2015. Facile fabrication of novel SiO_2/g-C_3N_4 core–shell nanosphere photocatalysts with enhanced visible light activity. *Applied Surface Science*, *357*, 346-355. https://doi.org/10.1016/J.APSUSC.2015.09.041.
[47] Zeng, Z., Mei, B. A., Song, G., Hamza, M., Yan, Z., Wei, Q., and Xiong, R. 2024. Physical interpretation of the electrochemical impedance spectroscopy (EIS) characteristics for diffusion-controlled intercalation and surface-redox charge storage behaviors. *Journal of Energy Storage*, *102*, 114021. https://doi.org/10.1016/J.EST.2024.114021.
[48] Bahadır, E. B., and Sezgintürk, M. K. 2016. A review on impedimetric biosensors. *Artificial cells, nanomedicine, and biotechnology*, *44*(1), 248-262. https://doi.org/10.3109/21691401.2014.942456
[49] Damjanovic, A., and Jovanovic, B. 1976. Anodic oxide films as barriers to charge transfer in O_2 evolution at Pt in acid solutions. *Journal of The Electrochemical Society*, *123*(3), 374-381. https://doi.org/10.1149/1.2132828
[50] Jothi, L., Jaganathan, S. K., and Nageswaran, G. 2020. An electrodeposited Au nanoparticle/porous graphene nanoribbon composite for electrochemical detection of alpha-fetoprotein. *Materials Chemistry and Physics*, *242*, 122514. https://doi.org/10.1016/J.MATCHEMPHYS.2019.122514.
[51] Giannetto, M., Elviri, L., Careri, M., Mangia, A., and Mori, G. 2011. A voltammetric immunosensor based on nanobiocomposite materials for the determination of alpha-fetoprotein in serum. *Biosensors and Bioelectronics*, *26*(5): 2232-2236. https://doi.org/10.1016/J.BIOS.2010.09.040.
[52] Liang, R. P., Yao, G. H., Fan, L. X., and Qiu, J. D. 2012. Magnetic Fe_3O_4@ Au composite-enhanced surface plasmon resonance for ultrasensitive detection of magnetic nanoparticle-enriched α-fetoprotein. *Analytica chimica acta*, *737*, 22-28. https://doi.org/10.1016/J.ACA.2012.05.043.
[53] Alizadeh, N., Salimi, A., and Hallaj, R. 2018. Magnetoimmunosensor for simultaneous electrochemical detection of carcinoembryonic antigen and α-fetoprotein using multifunctionalized Au nanotags. *Journal of Electroanalytical Chemistry*, *811*, 8-15. https://doi.org/10.1016/J.JELECHEM.2017.12.080.
[54] Lin, J., Wei, Z., and Mao, C. 2011. A label-free immunosensor based on modified mesoporous silica for simultaneous determination of tumor markers. *Biosensors and Bioelectronics*, *29*(1), 40-45. https://doi.org/10.1016/J.BIOS.2011.07.063.